

# Assimilation of Satellite Flood Likelihood Data Improves Inundation Mapping From a Simulation Library System

Article

**Published Version** 

Creative Commons: Attribution 4.0 (CC-BY)

Open Access

Hooker, H., Dance, S. L., Mason, D. C., Bevington, J. and Shelton, K. (2025) Assimilation of Satellite Flood Likelihood Data Improves Inundation Mapping From a Simulation Library System. Meteorological Applications, 32 (5). e70104. ISSN 1350-4827 doi: 10.1002/met.70104 Available at https://centaur.reading.ac.uk/125121/

It is advisable to refer to the publisher's version if you intend to cite from the work. See Guidance on citing.

Published version at: https://doi.org/10.1002/met.70104

To link to this article DOI: http://dx.doi.org/10.1002/met.70104

Publisher: John Wiley & Sons Ltd

All outputs in CentAUR are protected by Intellectual Property Rights law, including copyright law. Copyright and IPR is retained by the creators or other copyright holders. Terms and conditions for use of this material are defined in the <a href="End User Agreement">End User Agreement</a>.

www.reading.ac.uk/centaur



## **CentAUR**

Central Archive at the University of Reading Reading's research outputs online







# Assimilation of Satellite Flood Likelihood Data Improves Inundation Mapping From a Simulation Library System

Helen Hooker<sup>1</sup> Sarah L. Dance<sup>1,2,3</sup> D | David C. Mason<sup>3</sup> | John Bevington<sup>4</sup> | Kay Shelton<sup>4</sup>

<sup>1</sup>Department of Meteorology, University of Reading, Reading, UK | <sup>2</sup>Department of Mathematics and Statistics, University of Reading, Reading, UK | <sup>3</sup>National Centre for Earth Observation (NCEO), Reading, UK | <sup>4</sup>Jeremy Benn Associates Limited (JBA Consulting), Skipton, UK

Correspondence: Helen Hooker (helen.hooker@reading.ac.uk)

Received: 19 February 2025 | Revised: 28 July 2025 | Accepted: 15 September 2025

**Funding:** This work was funded in part by the Natural Environment Research Council as part of a SCENARIO funded PhD project with a CASE award from the JBA Trust (NE/S007261/1). S.L.D. and D.C.M. were funded in part by the EOCIS project. S.L.D. also received funding from NERC National Centre for Earth Observation.

Keywords: data assimilation | flood inundation | forecast-based financing | satellite data | simulation library

### **ABSTRACT**

Mitigating against the impacts of catastrophic flooding requires funding for the communities at risk, ahead of an event. Simulation library flood forecasting systems are being deployed for forecast-based financing (FbF) applications. The FbF trigger is usually automated and relies on the accuracy of the flood inundation forecast, which can lead to missed events that were forecast below the trigger threshold. However, earth observation data from satellite-based synthetic aperture radar (SAR) sensors can reliably detect most large flooding events. A new data assimilation framework is presented to update the flood map selection from a simulation library system using SAR data, taking account of observation uncertainties. The method is tested on flooding in Pakistan, 2022. The Indus River in the Sindh province was not forecast to reach flood levels, which resulted in no selection of the flood maps and no triggering of the FbF scheme. Following observation assimilation, the flood map selection could be triggered in four out of five sub-catchments tested, with the exception occurring in a dense urban area due to the simulation library flood map accuracy here. Thus, the analysis flood map has potential to be used to trigger a secondary finance scheme during a flood event and avoid missed financing opportunities for humanitarian action.

### 1 | Introduction

The warmer climate is increasing the frequency and intensity of extreme weather events as well as the exposure and vulnerability of communities and individuals (Pörtner et al. 2022). Large-scale flood forecasting systems predicting flood inundation extent are increasingly used for disaster risk reduction to improve preparedness ahead of a major flooding event (Stephens and Cloke 2014; Hooker et al. 2023b; Wu et al. 2020). An ensemble flood forecasting system creates probabilistic flood maps indicating the likelihood of flooding across a region or country. Flood impact risk factors such as population density, land-use

types or vulnerable infrastructure can also be mapped for the same area. The forecast-flood-likelihood maps can be overlaid with impact maps and depending on the severity of the hazard and the level of impact, a risk profile can be determined. The flood risk profile can be used to inform forecast-based financing (FbF) schemes that enable the pre-release of funds based on the flood forecast, ahead of the flood event (Coughlan de Perez et al. 2015, 2016). Automation of FbF schemes is important for rapid action to take place to mitigate against flooding impacts. The skill of the flood forecasting system is key to *triggering* the FbF scheme. A *non-trigger* of FbF ahead of or during a flood event might prove catastrophic for those impacted.

This is an open access article under the terms of the Creative Commons Attribution License, which permits use, distribution and reproduction in any medium, provided the original work is properly cited.

© 2025 The Author(s). Meteorological Applications published by John Wiley & Sons Ltd on behalf of Royal Meteorological Society.

Advanced flood forecasting systems, both at global and local levels, link together meteorological and hydrological forecasts of river discharge that drive the selection of pre-computed flood maps from a simulation library (Speight et al. 2021; Hooker et al. 2023a). The use of a simulation library obviates the need to run a hydrodynamic model as part of the forecast process, reducing computation time and allowing near real-time updating for large areas, which otherwise presents a significant computational challenge. The flood maps within the library are at a relatively higher spatial resolution (e.g., 30 m) compared to the resolution of the driving global hydrological model (e.g., approximately 5 km). This mismatch in scales can lead to problems with flood map selection and can cause gaps where the minimum return period threshold has not been exceeded (a non-trigger) by the forecast discharge (Hooker et al. 2023b). The three main issues that cause this in the global scale model are the representation of river networks, the return period thresholds determined and the exclusion of dam operations. Rivers that are narrower than a particular width, or catchment areas smaller than a pre-determined size are not resolved by global scale models. In addition, the return period thresholds set may be poorly calibrated due to a lack of ground truth observational data such as river discharge or river water level (Boelee 2022; Matthews et al. 2022). These two limitations can lead to a nontrigger, that is, no flood map is selected from the simulation library for a particular sub-catchment. Also, local dam operations such as diversions of river water for irrigation purposes or rapid releases of flood waters downstream, are not generally included in global scale models. This can lead to over- or under-prediction of forecast discharge, resulting in inaccurate or non-trigger of flood map selection in the forecast.

Satellite-derived observations of flooding have the potential to bring additional spatial information into flood inundation forecasts compared to in situ point gauging stations. These observations could be used to update and improve the FbF scheme either as part of a secondary finance payment following the acquisition of the satellite data or to improve the flood inundation forecasts going forwards as the flood event evolves. Synthetic aperture radar (SAR) sensors are particularly useful for remote flood detection, since they can see through cloud, most weather and are active both day and night (Mason et al. 2012; Schumann et al. 2023). Previously, SAR data have been used in several different ways to improve hydraulic models and flood prediction through data assimilation (DA). DA finds an optimal state (such as water level) or model parameter values by accounting for the previous forecast, the observations available, and both of their associated uncertainties. The updated state (analysis) or parameter set are used to initiate the next forecast in a feedback loop or cycle. A review of approaches used to assimilate satellitederived data into hydraulic models (from 2007 until 2015) can be found in tab. 7 of Grimaldi et al. (2016) and tab. 1 of Revilla-Romero et al. (2016).

When building a new DA system, there are some fundamental choices that have to be made, including the choice of underlying DA method. Several different DA methods have been used for flood inundation studies including ensemble Kalman filters (García-Pintado et al. 2013, 2015; Andreadis and Schumann 2014; Cooper et al. 2018; Annis et al. 2022; Nguyen et al. 2023), particle filters, (Hostache et al. 2018; Dasgupta,

Hostache, Ramsankaran, et al. 2021; Di Mauro et al. 2021, 2022) and variational techniques (Lai et al. 2014; Pujol et al. 2022). Variational assimilation solves an optimization problem, finding the single solution that maximises the posterior probability, given the observations and their uncertainties (Lorenc et al. 2000).

A second fundamental choice in building a new DA system, is the approach for comparing the model data to the observations. For SAR observations, a first step is often to extract flood extent using an image classification technique (see Section 3, Grimaldi et al. (2016)). The flood extent information could be directly assimilated, as a binary flood map (e.g., Lai et al. 2014). An alternative is to intersect the edge of the binary flood map with a digital elevation model (DEM) and derive a water level observation (Mason et al. 2007, 2012). SAR-derived water levels only provide information at the flood edge and rely on the spatial resolution and the vertical accuracy of the underlying DEM (Dasgupta, Hostache, Ramasankaran, et al. 2021), which makes them difficult to obtain. Nevertheless, water level observations can provide more long-lasting impact than binary flood extents in DA cycling systems (Cooper et al. 2019). Probabilistic flood mapping procedure for SAR data was first introduced by Giustarini et al. (2016). This created the potential for flooding probabilities to be assimilated directly via particle filter approaches (e.g., Dasgupta, Hostache, Ramsankaran, et al. 2021; Di Mauro et al. 2021, 2022). More recently, observation uncertainty associated with classifying flood extent from SAR data is openly available through the Copernicus Management Service (CEMS) (Copernicus Programme 2021) with a time lag of less than 8 h between satellite data acquisition and the generation of flood maps.

All of these previous studies involved the assimilation of satellitederived data to update hydrodynamic model states or parameter values by taking a DA cycling approach. The assimilation provides updated initial conditions ahead of the next forecast cycle. The new approach here differs significantly by aiming to develop a DA framework to assimilate probabilistic flood maps into a simulation library flood inundation forecasting system. A variational approach is taken as it is particularly suited to a simulation library system. The set of states ranged over in the optimization process can be limited to the pre-computed solutions in the library. This ensures that the resulting analysis flood map remains consistent with the flood forecasting system. The goal is to improve flood map selection by creating a new analysis flood map. Spatially distributed flood likelihood information derived from SAR data is used within the DA framework. It is important to note that this DA approach does not include a feedback loop to the forecasting system. The DA framework is tested using forecast data and optical satellite observations from a major flood event in Pakistan, August 2022. (Floodlist 2022).

In this article, the flood forecasting system and derivation of the static simulation library along with satellite-derived observations of flood likelihood are outlined in Section 2. The development of a new DA method is described in Section 3. Recently published verification methods that are used to evaluate the results are described in the same section (Hooker et al. 2022, 2023a, 2023b). Section 4 presents an overview of the 2022 Pakistan flood and details of the data used. The observation data includes subcatchments where the flooding is well observed, but also dense

urban areas, which are masked out in the flood likelihood product as they are deemed unsuitable for SAR-derived flood detection. The DA framework successfully triggered flood maps in 4 out of 5 sub-catchments tested as shown in the results, discussed in Section 5. Section 6 concludes with recommendations for future work to improve the use of SAR flood likelihood data to update a simulation library flood forecasting system through DA.

### 2 | Simulation Library Forecasting System and Observation Data

Flood Foresight, a simulation library flood inundation forecasting system and its application for disaster risk reduction through FbF, is outlined in Section 2.1 (Revilla-Romero et al. 2017). Section 2.2 details the derivation of the flood likelihood data from SAR that will be used as observation data in the assimilation process. The extraction of flood extent information from optical images that will be used for validation is explained in Section 2.3.

# 2.1 | Flood Foresight and Forecast-Based-Financing

The chain of flood forecasting systems used to predict flood inundation and to produce flood impact forecasts are detailed in Figure 1. The Global Flood Awareness System (GloFAS) couples global ensemble weather forecasts with a hydrological model and provides daily ensemble forecast river discharge at approximately 10 km grid size (v3.2, GloFAS 2021). The GloFAS forecast river discharge is used to as an input to drive the Flood Foresight system. Flood Foresight (Revilla-Romero et al. 2017; Hooker et al. 2023a) is a fluvial, probabilistic flood inundation forecasting system. Flood Foresight is set up by dividing the catchment into 'Impact Zones' (IZ) or sub-catchments using the HydroBASINS data set (Lehner 2014). Each IZ in Flood Foresight is linked to a GloFAS grid cell that provides a 51 ensemble member forecast of river discharge. Flood Foresight contains a simulation library of precomputed flood depth and extent maps. The flood map library was hydrodynamically modelled using JFlow, (Bradbrook 2006) and RFlow using a detailed 30 m digital surface model. The maps were modelled at specific return period thresholds (20, 50, 100, 200, 500, and 1500 years). Subsequently, these were linearly interpolated at 5 intermediate intervals between each return period threshold and extrapolated between zero and the 20 year return period flood map (totalling 36 flood maps). Depending on the forecast discharge from GloFAS for each IZ, a flood map is selected from the simulation library. The flood map selected is determined by the return period threshold exceeded within each IZ. The resultant forecast flood map is created by stitching together individual IZ flood maps (at various RPs) and is produced daily out to 10 days ahead.

The charity Start Network (Start Network 2022) brings together a group of over 80 humanitarian agencies and aims to develop local community-led, early action through a model of proactive funding to mitigate against the impacts of crises. JBA Consulting, in partnership with Start Network, have developed a disaster risk financing system for the Indus River basin in Pakistan that links Flood Foresight forecast flood maps to populations impacted by flooding (Figure 1). For the purposes of setting FbF trigger threshold levels, the disaster risk financing system quantifies the flood risk to the population through a commercial probabilistic global catastrophe risk model, FLY (Dunning 2019). The dynamic operational index triggering could be linked to the analysis flood map (produced here as a result of the DA) to provide a secondary finance payment.

### 2.2 | Satellite-Derived Flood Likelihood

The Copernicus global flood monitoring (GFM) is an open source service that combines the outputs of three different algorithms to extract flood extent and uncertainty information from Sentinel-1 SAR data (GloFAS Global Flood Monitoring (GFM) 2021). The process is automatic and runs continuously in near real-time (within 8 h after image acquisition) for every SAR image detecting flooding on a global-scale. The resulting flood information layers are available through open access. The mini-ensemble approach used for flood detection increases the confidence in the resulting derived observations. The first flood mapping algorithm developed by the Luxembourg Institute of Science and Technology uses a pair of SAR images (pre-flood and flood) and a hierarchical split-based change detection approach to classify permanent and flood waters

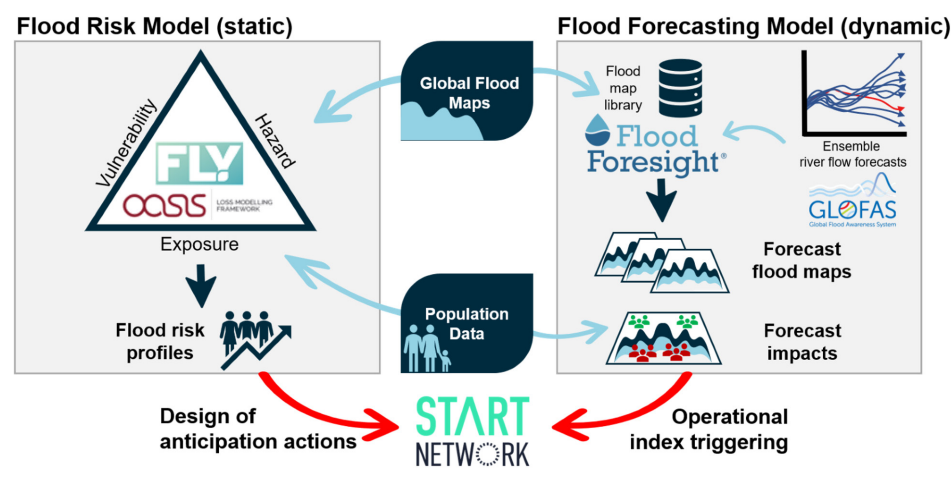


FIGURE 1 | Flood foresight/start network ensemble flood inundation forecasting and disaster risk financing system.

Meteorological Applications, 2025 3 of 13

(Chini et al. 2017). The classification uncertainty depends on the Bayesian inference classification probabilities. The second flood mapping algorithm by the German Aerospace Research Centre uses a hierarchical tile-based thresholding approach and the optimization of the classification by combining various information sources using fuzzy-logic theory and region growing (Martinis et al. 2015; Twele et al. 2016). The uncertainty information depends on fuzzy memberships. The final algorithm from the Vienna University of Technology uses the historical time series of the SAR backscatter values per pixel and classifies flood extent from the backscatter probability distribution (Wagner et al. 2020; Bauer-Marschallinger et al. 2022). The classification uncertainty is based on the Bayesian posterior probability. The output flood layer is derived using the miniensemble with a pixel classified as flooded where two out of three of the algorithms determines a flood class. The flood likelihood values are aggregated, first by converting each to lie in the same range [0, 100] before averaging the likelihood values. Regions where SAR is unable to detect flooding due to shadow or layover effects are removed from the classification process. This usually includes dense urban areas, densely vegetated areas, regions with steep slopes and regions that might appear flooded such as dry, sandy desert-like surfaces. The exclusion mask is available to download as an additional layer. Permanent and seasonal water bodies are classified separately as a reference water mask layer.

Krullikowski et al. (2023) applied and assessed the usefulness of GFM ensemble likelihood on two test sites in Myanmar and Somalia, both situated in challenging areas for flood detection using SAR data. Krullikowski et al. found that the GFM ensemble likelihood layer resulted in improved trust in the ensemble flood extent detection approach and provides more reliable and robust uncertainty information for detecting flooding compared to using a single algorithm only.

# 2.3 | Optical Normalised Difference Water Index (NDWI)

Occasionally, optical satellite data can be useful for observations of flood extent. Flood detection from optical satellites depends on a near cloud-free sky where the satellite acquisition coincides with the flood event. The Normalised Difference Water Index (NDWI) for flood and surface water detection is calculated with Sentinel-2 optical data using the green band (B03,  $\approx 560$  nm) and the near infrared band (B08,  $\approx 842$  nm) (Albertini et al. 2022). The NDWI is given by:

$$NDWI = \frac{B03 - B08}{B03 + B08},\tag{1}$$

where positive values indicate water. Albertini et al. (2022) reviewed the performance of surface water and flood detection metrics using multispectral satellite data. They found that the average overall accuracy from previous flood studies applying NDWI to be 87.85% and for permanent surface water studies scored 94.41%. This included studies using data from different satellite sensors with spatial resolutions ranging from 10 m for Sentinel-2 to 500 m for Terra-Aqua Moderate Resolution Imaging Spectroradiometer (MODIS, Justice et al. (2002)).

### 3 | Methods

### 3.1 | Data Assimilation Framework

The aim of the DA framework is to update a previous forecast of flood inundation extent and depth from Flood Foresight (the background) where a non-trigger has occurred in the forecast system but where flooding was derived from concurrent satellite-based SAR data. Using observation uncertainty information from the GFM flood likelihood layer (explained in Section 2.2), the objective is to improve the flood map selection for non-triggered IZ by minimising a cost function per IZ (Figure 2).

The DA framework aims to update the state vector,  $\mathbf{x} \in \mathbb{R}^n$ , which contains flood depths at each grid cell location. The components of  $\mathbf{x}$ ,  $x_i$ , are the individual flood depths for a specific grid cell location. The total number of grid cells across an IZ is n, the total of observed unmasked grid cells is m. To find the optimum state accounting for observation uncertainty the observation likelihood term is defined  $P(\mathbf{y}|\mathbf{x})$  where the components of observations,  $\mathbf{y} \in \mathbb{R}^m$  have two possible binary outcomes,  $y_i = 1$  (flooded) and  $y_i = 0$  (unflooded), following classification from SAR data. The likelihood term can be represented by a Bernoulli distribution (Lauritzen 2023), defined as:

$$P(\mathbf{y}|\mathbf{x}) = \prod_{i=1}^{m} L_i^{[\mathbf{H}(x)]_i} (1 - L_i)^{1 - [\mathbf{H}(x)]_i},$$
(2)

where  $L_i$  is the GFM flood likelihood value (see Section 2.2). The i-th component of the observation operator  $\mathbf{H}(\mathbf{x})$ , defined as

$$[\mathbf{H}(\mathbf{x})]_i = \begin{cases} 1 & \text{flooded } x_i > 0.2m \\ 0 & \text{unflooded otherwise} \end{cases}, \tag{3}$$

acts to convert flood depths (state space) to a binary flood class (observation space) at unmasked grid cells, excluding observation likelihood information for masked grid cells where SAR data cannot reliably detect flooding. To find the maximum

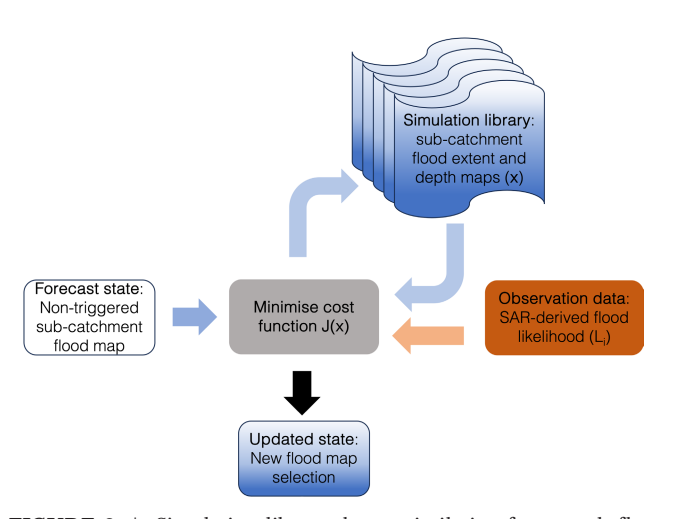


FIGURE 2  $\mid$  Simulation library data assimilation framework flow diagram.

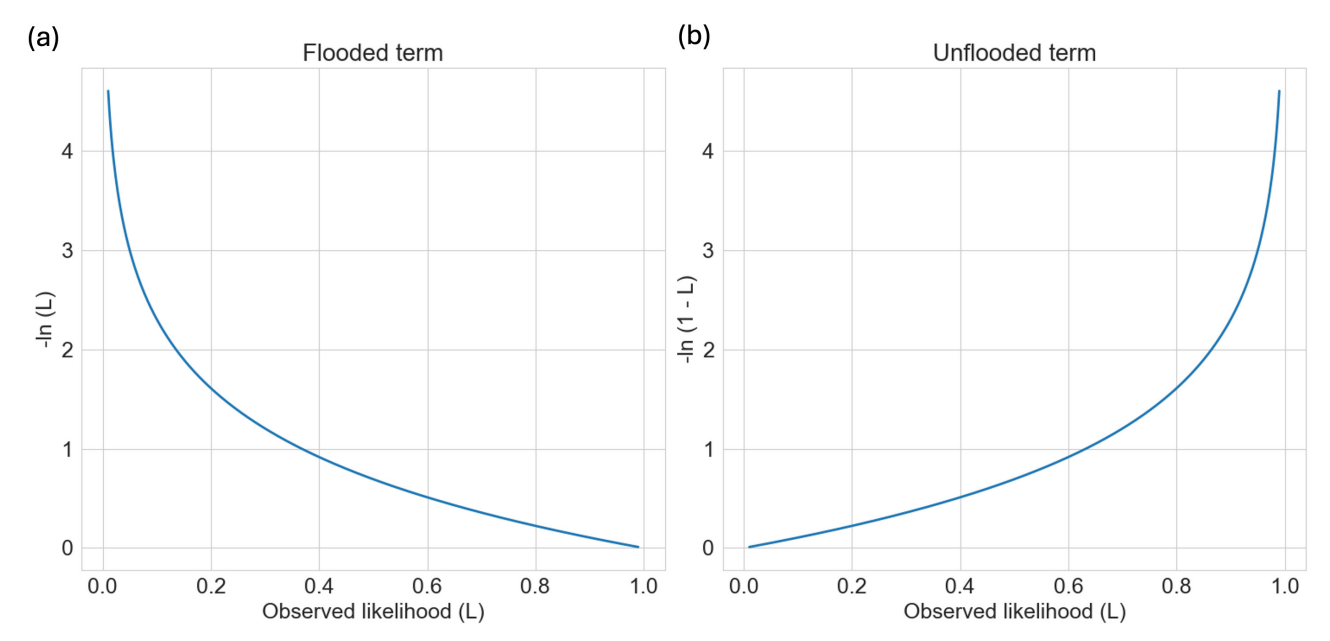


FIGURE 3 | Negative log loss function relationship with observed flood likelihood for flooded (a) and unflooded (b) grid cells.

posterior likelihood of the state variable, the negative log likelihood of  $P(\mathbf{y}|\mathbf{x})$  is taken and divided by the number of unmasked grid cells m to derive the cost function (averaged across unmasked grid cells per IZ)

$$J(\mathbf{x}) = -\frac{1}{m} \sum_{i=1}^{m} \left\{ [\mathbf{H}(\mathbf{x})]_{i} \ln(L_{i}) + (1 - [\mathbf{H}(\mathbf{x})]_{i} \ln(1 - (L_{i})) \right\}, (4)$$

$$J(x) = -\frac{1}{m} \sum_{i=1}^{m} \underbrace{\{ [\boldsymbol{H}(\boldsymbol{x})]_{i} \operatorname{In}(\boldsymbol{L}_{i}) + (1 - [\boldsymbol{H}(\boldsymbol{x})]_{i} \operatorname{In}(1 - (\boldsymbol{L}_{i})) \}.}_{\text{inflooded}}$$
(5)

The cost function in Equation (4) has a similar derivation to conventional three-dimensional variational DA, but its form is different since, unlike conventional variational DA, the observation likelihood is not Gaussian. The cost function in Equation (5) adds labelled terms to Equation (4) for a binary flooded or unflooded application. One term on the right-handside of Equation (5) is calculated per grid cell depending on whether the corresponding grid cell in the flood map library is flooded or unflooded. The relationship between the loss function and the observed likelihoods is plotted in Figure 3. For flooded grid cells, high probability values are penalised less heavily compared to low probability values, the opposite is true for unflooded grid cells. The value of  $J(\mathbf{x})$  is calculated per IZ by iterating through the flood map library (36 flood maps) and finding the flood map return period by minimising  $J(\mathbf{x})$ , which is equivalent to maximising the posterior likelihood, given the observation uncertainty data. To ensure that the minimum is reached across the flood map library,  $J(\mathbf{x})$  is calculated for all 36 flood maps. Note that this is different to the standard DA approach where minimisation would be accomplished via a gradient descent algorithm (Bannister 2017). However, the approach does have an analogy with conventional strongconstraint four-dimensional variational DA, where the solution must fit the forecast model.

Following the assimilation process, replacing the non-triggered IZ with updated flood maps results in an analysis flood depth and extent map (the flood depth information is contained within the simulation library). This means that the analysis flood map remains consistent with the Flood Foresight system where the flood maps have been hydrodynamically modelled, that is, they are physically realistic. Retaining the flood depth information is important for FbF applications for quantifying the risk of flood impacts. Since the observations have binary values (flooded/unflooded), it is not possible to distinguish between floods that have the same extent but different depths from the observation data. This property is inherited in the cost function. The cost function computation time per IZ for 36 flood maps takes an order of seconds on a laptop. By utilising parallel processing, multiple IZs could be computed simultaneously enabling near real-time implementation across a region in an operational environment.

### 3.2 | Validation Methods

The resulting analysis flood map, following assimilation of SAR-derived flood likelihood data, is validated by comparing against independent flood extent observation data derived from optical satellite data, the NDWI (Section 2.3). The results will be validated by calculating the Fraction Skill Score (FSS, Roberts and Lean (2008); Hooker et al. (2022)) and by mapping the performance on a Categorical Scale Map (CSM, Dey et al. (2014); Hooker et al. (2022, 2023a)). Both the FSS and the CSM avoid issues with the double penalty impact of conventional binary performance measures as well as the impact of flood magnitude on the skill score (Hooker et al. 2022). The FSS is based on the Brier Skill Score and uses a neighbourhood approach to determine the skillful spatial scale of the analysis flood map. The fraction of flooding within a given square neighbourhood size of length n is compared by calculating the mean-squared-error (MSE) between the analysis and the validation flood maps to give

Meteorological Applications, 2025 5 of 13

$$FSS_n = 1 - \frac{MSE_n}{MSE_{n(ref)}},$$
(6)

where  $\mathrm{MSE}_{n(\mathrm{ref})}$  is a potential maximum MSE that depends on the fraction of flooding across the IZ on the analysis and the validation flood maps. A skilful scale is determined when FSS  $\geq$  FSS $_T$ , the target FSS score, where FSS $_T \geq 0.5 \frac{f_o}{2}$  depends on the fraction of observed flooding across the IZ,  $f_o$ . When the analysis and validation flood extents are equal in area across an IZ there is said to be no background bias and the maximum FSS is 1. Otherwise, the maximum asymptotic FSS (AFSS) is given by:

$$AFSS = \frac{2f_0 f_a}{f_0^2 + f_a^2},\tag{7}$$

where  $f_a$  is the fraction of flooding on the analysis flood map per IZ.

The CSM plots a local agreement scale (S) at every grid cell. An overview of the method is presented here. Please see Dey et al. (2014); Hooker et al. (2022, 2023a) for full details of the methodology. A background bias between the analysis and verification flood maps that is deemed acceptable is predetermined. The pre-set bias is used to calculate an agreement criterion that must be reached by the flood map comparison calculation. The comparison begins at each grid cell n=1, if the agreement criterion is met at grid level, the grid cell is labelled with an agreement scale S=0. Where the criterion is not met, a larger neighbourhood size is compared (e.g., n=3). The fraction flooded in each of the analysis and validation flood maps are compared and if the criterion is met, the agreement scale assigned would be S=1. The process continues to larger neighbourhoods (e.g.,

n=7, S=3) until either the criterion is met or a predetermined limit is reached ( $S_{lim}$ , set to 9 for this application). The agreement scale at this limit would indicate a false alarm or miss for the grid cell. Note that the relationship between n, the neighbourhood size used for the FSS, and S is given by S=(n-1)/2. The agreement scales are combined with data from a conventional contingency map (indicating whether the flood map grid cell is over- or under-estimating flooding, Stephens et al. (2014)) and are mapped across an IZ. The CSM indicates a location-specific level of agreement and shows where the flood maps are over-or under-estimating flooding. Grid cells coloured red indicate under-estimation, while blue grid cells indicate over-estimation.

### 4 | Pakistan Flood 2022

### 4.1 | Event Overview

In Spring 2022, Pakistan experienced a record-breaking heatwave with temperatures exceeding 50°C. The heat exacerbated upstream glacial snow melt feeding the Indus River basin, which runs over 3000km across the length of Pakistan, draining the Himalayas to the Arabian Sea. An intense monsoon season followed in July and August, driving multiple flood-producing mechanisms including multi-day extreme precipitation that was the primary driver of floods (World Weather Attribution 2022; Nanditha et al. 2023). Attribution studies indicate that the 5-day maximum rainfall over the provinces Sindh and Balochistan, which led to catastrophic flooding, was made 75% more intense by 1.2°C of global warming (World Weather Attribution 2022). The northern Sindh province received an estimated 442.5 mm of rainfall in August, 784% more than usually recorded, causing inundation of 55,000 km<sup>2</sup> across the region (Floodlist 2022). Despite early warnings of the potential for significant flooding from GloFAS, the unimaginable scale and

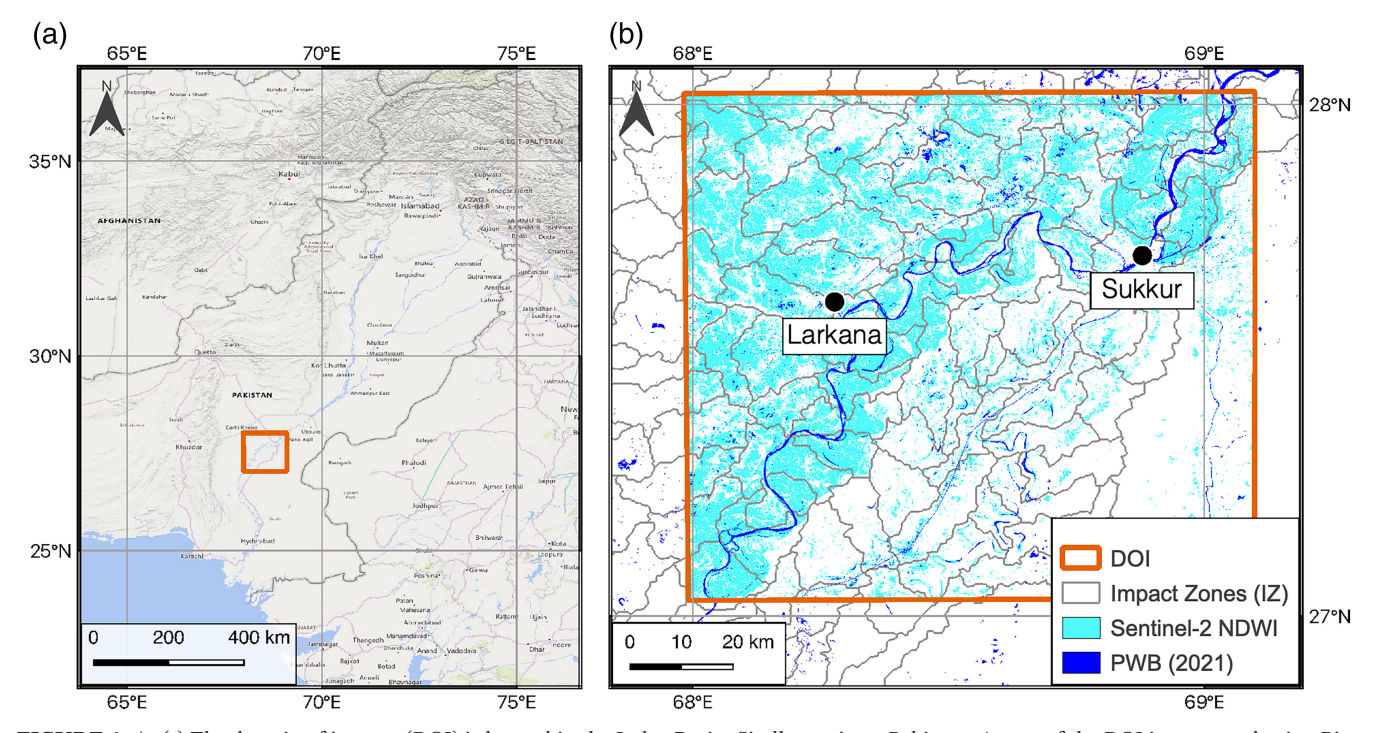


**FIGURE 4** | (a) The domain of interest (DOI) is located in the Indus Basin, Sindh province, Pakistan. A map of the DOI is generated using Bing Maps. 2024 Microsoft Corporation. (b) The region is divided into sub-catchments or Impact Zones (IZ) in Flood Foresight. Satellite-derived flooding (NDWI) from Sentinel-2 data (Section 2.3) from 31 August 2022 is highlighted along with permanent water bodies (PWB).

6 of 13 Meteorological Applications, 2025

magnitude of the flood impacted over 33 million people with over 1700 lives lost and costing more than \$40 billion in economic damages (Floodlist 2022; World Resources Institute 2023).

### 4.2 | Data

The DA framework (Section 3.1) was tested in the northern Sindh province where widespread flooding occurred during August 2022. Figure 4 maps the NDWI derived from Sentinel-2 optical data (Section 2.3) that was used to verify the resultant analysis flood map following DA. Local reports and photographs of flooding were made in the cities of Sukkur and Larkana (DAWN 2022; The Guardian 2022; Sky News 2022). The DA was applied to 5 IZ covering 3 different scenarios (Figure 5): (1) One IZ where a large proportion of the IZ is a dense urban area and is masked (where the GFM product is currently unable to detect flooding), Sukkur (S), see Figure 5a; (2) Two IZ with mixed urban and rural areas, Larkana north and south (LN, LS); and (3) two flood edge locations (FE1, FE2). The GFM

flood likelihood data used to represent observation uncertainty in the DA is mapped in Figure 5a where darker shades of orange indicate a higher likelihood of flooding (Section 2.2). The forecast data from Flood Foresight is mapped in Figure 5b where the purple shades indicate the maximum return period flood map triggered by the system from 10 to 31 August, 2022. Each of the IZ selected were non-triggered IZ during this period. The driving forecast river discharge data from GloFAS did not reach the required threshold to trigger a flood map along the central Indus channel. This is likely due to poor calibration of GloFAS due to a lack of observation of river stage or discharge. The Sukkur barrage operations for diversion and altering of river water flows are not currently included in the GloFAS system, which makes forecasts unreliable along this stretch of the Indus River.

### 5 | Results and Discussion

Results are presented for the 3 scenarios tested in the following section. The benefits and limitations of the approach are

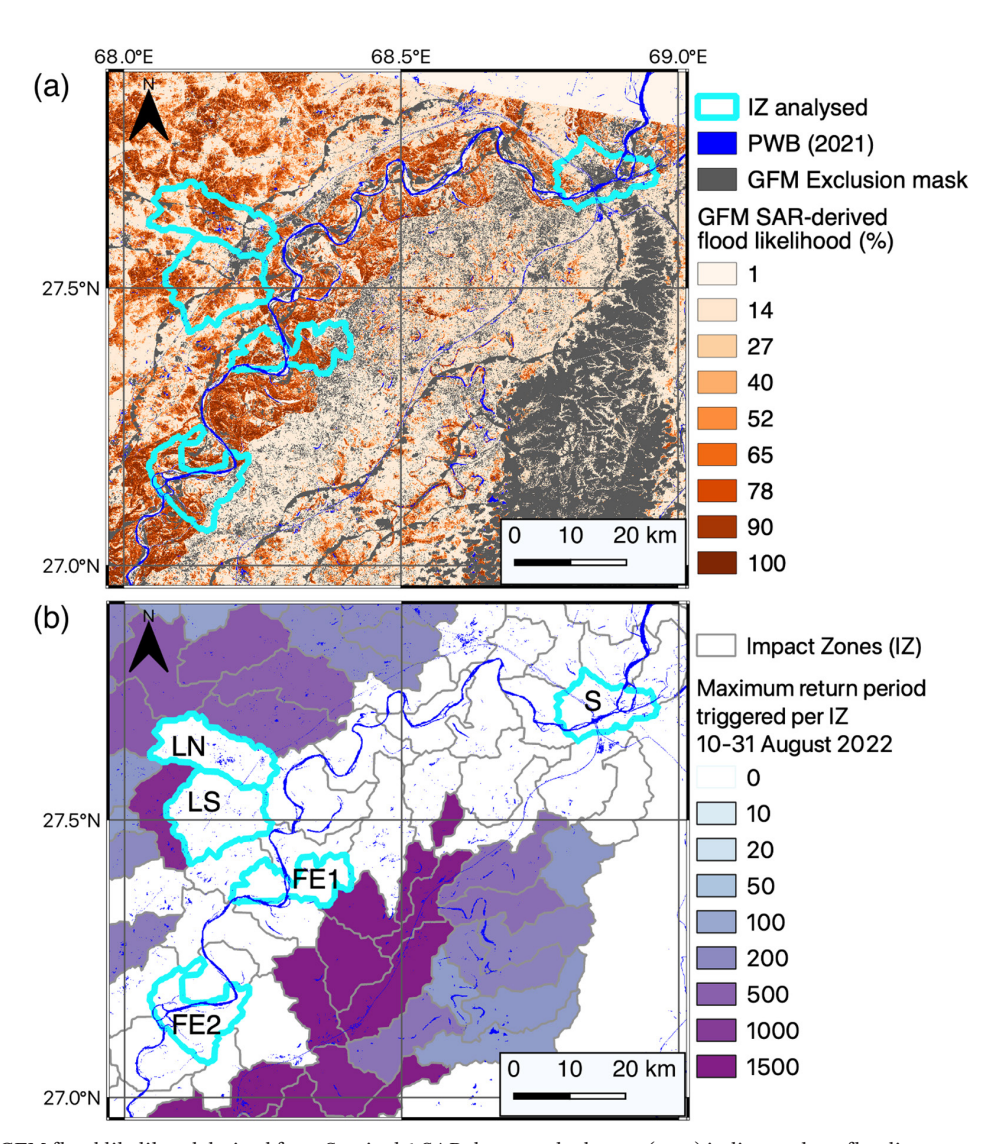


FIGURE 5 | (a) GFM flood likelihood derived from Sentinel-1 SAR data, masked areas (grey) indicate where flooding cannot be reliably detected from SAR data. (b) The maximum return period threshold triggered per IZ by the Flood Foresight system during peak flooding 10–31 August 2022. Five non-triggered IZ of interest labelled: S—Sukkur, LN—Larkana North, LS—Larkana South, FE1—flood edge 1, FE2—flood edge 2. Note that PWB means permanent water bodies.

Meteorological Applications, 2025 7 of 13

discussed and how the method could potentially be modified for improved performance.

### 5.1 | Scenario 1

The DA framework was applied to 3 different scenarios totalling 5 IZ. The first scenario tested was an IZ centred on the city of Sukkur. Sukkur is located just south of a large barrage, used to control flood waters. Significant flooding was observed locally in the Sukkur region (Sky News 2022), however the dense city centre means that flooding is difficult to detect using Sentinel-1 imagery at 20 m spatial resolution. Around one third of the IZ is masked by the GFM process (Figure 6c) but high flood likelihood values are visible across some areas of the IZ (Figure 5a). The aim is to test whether the DA framework can select a flood map from the simulation library based on limited usable SAR data.

The value of the cost function  $J(\mathbf{x})$  from Equation (4), Section 3.1 is plotted against the return period value of each flood map from the simulation library in Figure 6a. The cost function was minimised at the lowest return period flood map (3 years) and a 'no flood' map gave a slightly lower value of  $J(\mathbf{x})$ . In this instance, the lower return period flood maps over-estimated flooding in areas where low flood likelihood values were derived from SAR. The influence of the Sukkur barrage and river canals running across the IZ made the hydrodynamic modelling more difficult.

Also, the flood maps do not include local defence information and the flood map interpolation process is highly uncertain at return periods less than 20 years. The results mean that no flood map was triggered following the DA (Figure 6b,c) with the CSM map (Figure 6d) indicating where the flooding was underestimated, particularly upstream of the Sukkur Barrage, with no flood map selected.

### 5.2 | Scenario 2

The second scenario focused on a mixed urban and rural area with 2 IZ chosen around Larkana city. The dense urban area is again masked and is split across the 2 IZ (Figure 5a), but there are large unmasked areas with high and low flood likelihood values. The assimilation results for scenario 2 are plotted in Figure 7a where the cost function minimum value is similar for both LN and LS with a 7 year return period flood map triggered for LN and a 13 year return period flood map triggered for LS (Figure 7b). The resultant analysis flood maps selected (Figure 7c) also indicate flooding within Larkana city, overlapping the masked area. This is consistent with local observations and is important for population impact calculations for FbF schemes. The CSM indicates that whilst a large area is now correctly indicating flooding there are also large areas that are under-estimated by the analysis flood map (Figure 7d). The neighbouring IZ that were triggered by the forecast system (Figure 7b) are at much higher return period thresholds than

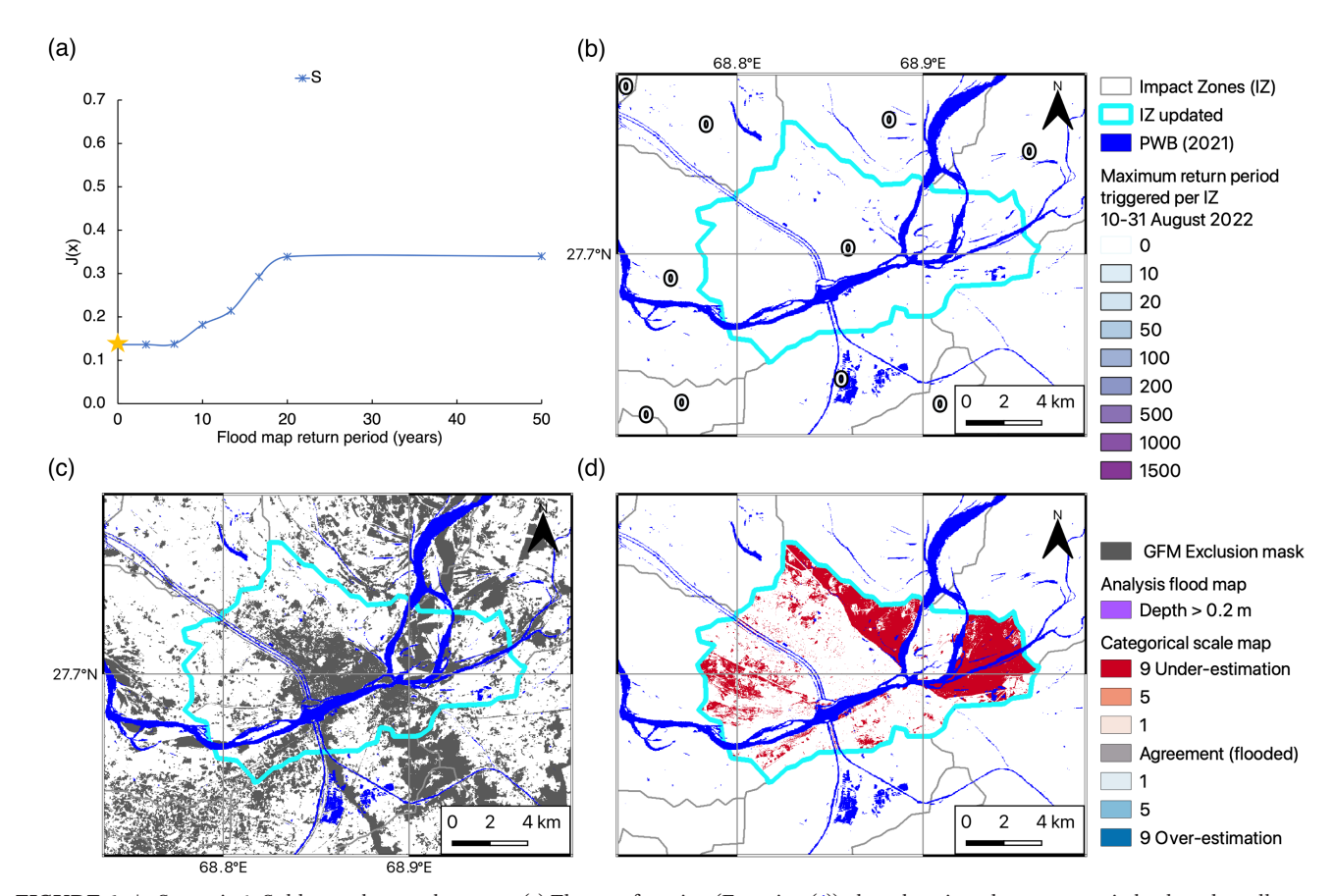


**FIGURE 6** | Scenario 1: Sukkur, a dense urban area. (a) The cost function (Equation (4)) plotted against the return period value, the yellow star highlights the minimum value of J(x). (b) The analysis return period triggered following DA. (c) The analysis flood extent map (note that no map was triggered for Sukkur) and (d) the CSM comparing the analysis flood extent map against Sentinel-2 NDWI.

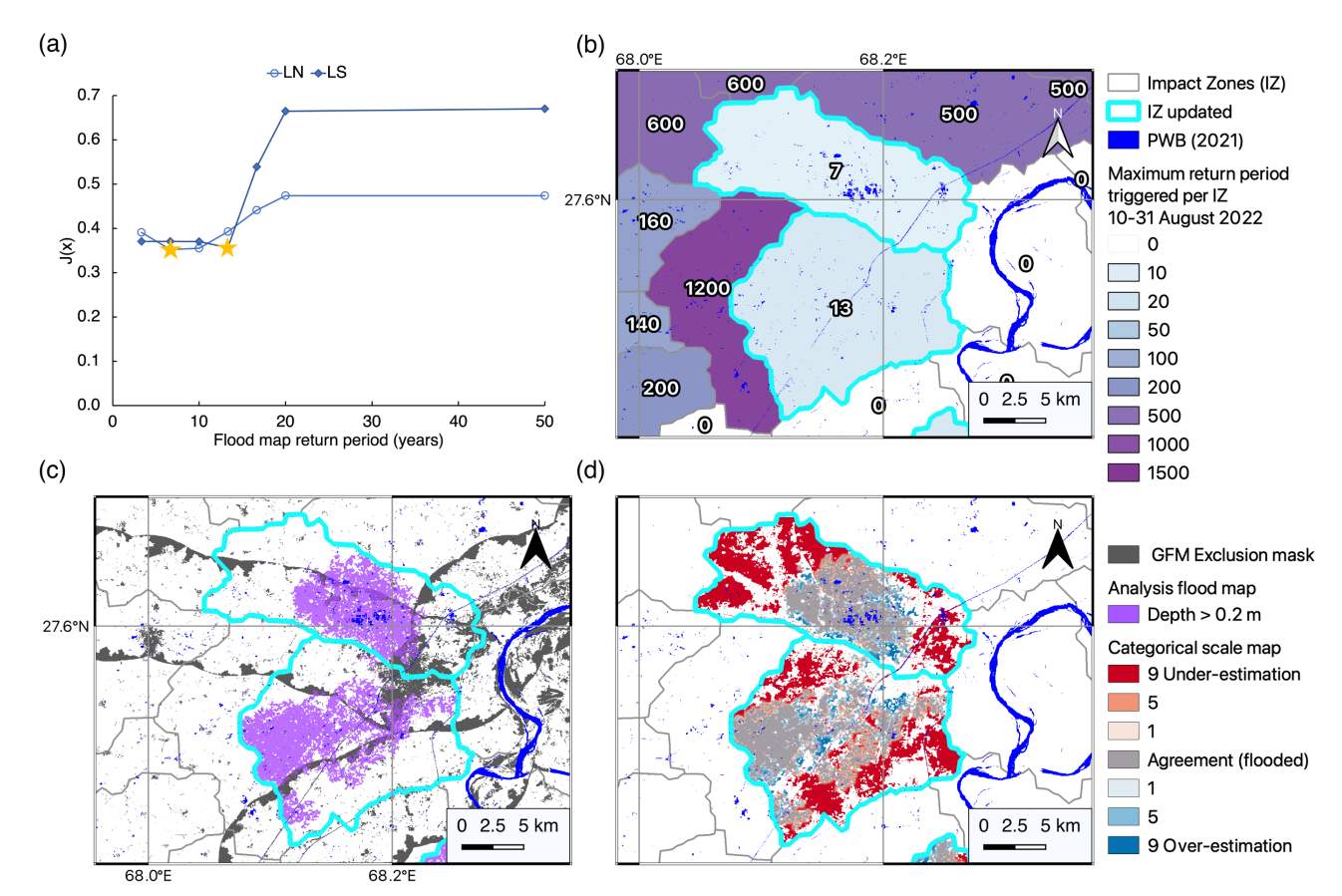


**FIGURE 7** | Scenario 2: Larkana, a mixed urban and rural area. (a) The cost function (Equation (4)) plotted against the return period value, the yellow star highlights the minimum value of J(x). (b) The analysis return period triggered following DA. (c) The analysis flood extent map and (d) the CSM comparing the analysis flood extent map against Sentinel-2 NDWI.

the ones selected following the DA. By inspecting higher return period flood maps than those selected by the DA (for LN and LS) it became clear that these were over-estimating flooding in locations where low flood likelihood values were located causing J ( $\mathbf{x}$ ) (Figure 7a) to increase.

One potential solution to the inconsistency seen across the domain could be overcome by including information from the forecast system. The assimilation process could be carried out across a region including multiple IZ at the same time, rather than considering individual IZ. Conditions could be imposed, such as a consistent flood depth across IZ boundaries away from the flood edge. One way to impose some smoothness would be through the use of a background error term. Note that the background error is the prior or forecast error. Information from neighbouring IZ could be spread across a domain by the background error covariance (B) matrix used in variational DA (Bannister 2008). The matrix B could be calculated offline using the flood depth maps from the simulation library.

Once the entire IZ becomes inundated at a 20-year return period,  $J(\mathbf{x})$  remains constant with increasing return period (Figure 7a). Although the depth values are increasing, there are no significant changes in flood extent possible across the IZ, meaning the cost function cannot distinguish between flood maps over a 20-year return period. For the IZ tested here, the minimum has already occurred at lower return period, but it is possible that the minimum could occur where  $J(\mathbf{x})$  is constant, meaning a range

of potential RPs are possible solutions. In order to distinguish between equally plausible flood maps, additional observation data would be required to measure flood depth. Flood depth data for sufficiently large floods could be derived from satellite altimetry data such as the Surface Water and Ocean Topography (SWOT) mission (Frasson et al. 2019; de Moraes Frasson et al. 2023).

### 5.3 | Scenario 3

The final scenario investigates the impact of assimilating SARderived flood likelihood data on flood map selection where the flood edge lies within the IZ. The cost function value of  $J(\mathbf{x})$  drops relatively sharply for FE1 in the north (Figure 8a) from 0.56 at 3 years return period to a minimum of 0.34 at 17 years return period. Further south,  $J(\mathbf{x})$  for FE2 is initially lower at 0.21 at 3 years return period, gradually decreasing to a minimum of 0.17 at 20 years return period. The shape of the cost function shows a smoother descent to a minimum compared to scenarios 1 and 2 as there is more variation in flood extent between flood maps at different RPs at the flood edge location. In similarity to scenario 2 (Larkana), neighbouring IZ are again at very high return period levels (Figure 8b). The analysis flood map for FE1 does not reach the edge of the IZ, whereas FE2 virtually flood fills the IZ (Figure 8c). The CSM (Figure 8d) shows that some flooding close to the main Indus River has been under-estimated in FE1 but with overall good accuracy and limited over-estimation. FE2 shows

Meteorological Applications, 2025 9 of 13

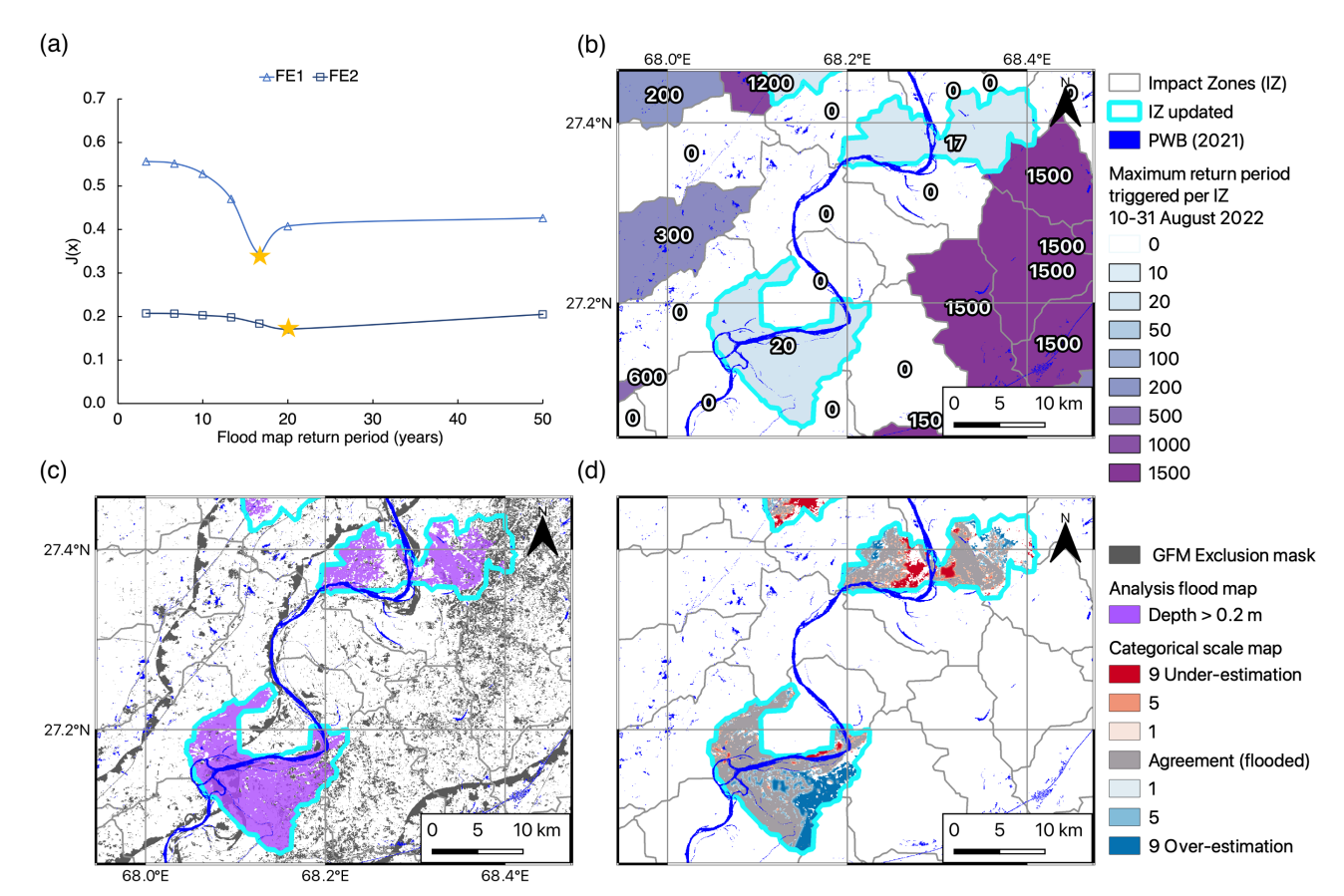


**FIGURE 8** | Scenario 3: Flood edge location. (a) The cost function (Equation (4)) plotted against the return period value, the yellow star highlights the minimum value of J(x). (b) The analysis return period triggered following DA. (c) The analysis flood extent map and (d) the CSM comparing the analysis flood extent map against Sentinel-2 NDWI.

TABLE 1 | Validation skill scores for each IZ analysis flood map compared against independent Sentinel-2 NDWI.

	Analysis return				
IZ code	period	FSS at $(n=1)$	$FSS_T$	AFSS	$n$ at $FSS_T$
S	0	0	n/a	n/a	n/a
LN	7	0.32	0.64	0.40	$AFSS < FSS_T$
LS	13	0.38	0.65	0.51	$AFSS < FSS_T$
FE1	17	0.55	0.66	0.71	$n = 35 (525 \mathrm{m})$
FE2	20	0.49	0.63	0.77	$n = 15 (225 \mathrm{m})$

Note:  $FSS_T$  is the target skill score and AFSS is the maximum asymptotic skill score. Note that without DA, no flood map would be triggered and all grid cells would be classed as unflooded; therefore, the FSS equals zero.

over-estimation in the west but again a large area in agreement with the flood extent derived from Sentinel-2 NDWI. Using flood extent observation likelihood data would be more useful where the flood edge stays within the IZ tested for the maximum return period flood map. There would be more chance of variation in the cost function value across the full range of return period flood maps. In contrast, for a (near) flood filled IZ there would be less variation seen in  $J(\mathbf{x})$  due to limited changes in flood extent. Future work could focus on assimilating flood edge IZ and sharing information with neighbouring IZ by including a background term to update regions closer to the river channel where the IZ are more likely to be flood filled (Section 5.2).

### 5.4 | Analysis Flood Map Validation

In Table 1 the FSS (Section 3.2) has been calculated by comparing the analysis flood map selected per IZ with the corresponding Sentinel-2 NDWI representing observed flooding, with permanent water bodies excluded from the validation. The target skill score  $FSS_T$  and the asymptotic FSS AFSS are also calculated. Prior to DA, when no flood map is selected, the flood inundation area is zero. Therefore, the FSS without DA equals zero. The FSS for scenario 1 (Sukkur) equals zero as no flood map was triggered. For scenario 2 (LN and LS) the FSS score at grid level n=1 (0.32 and 0.38) is around half of  $FSS_T$  Usually, by increasing the neighbourhood size the value of FSS also

increases, eventually exceeding  $FSS_T$ . In this case AFSS (which is calculated using the fraction flooded across the IZ from both the analysis and observed flood maps) is less than  $FSS_T$  meaning the total differences in flood extent are too large for the FSS to reach or exceed  $FSS_T$ . The result of this is that there is not a meaningful or skilful scale of the analysis flood maps for scenario 2. This is due to the under-estimation of flood extent seen on the CSM (Figure 7d). For scenario 3,  $FSS_T < AFSS$  which makes it possible to calculate a skilful scale where  $FSS \ge FSS_T$ . For FE1 this occurs when n=35 or 525 m and FE2 at n=15 or 225 m confirming that FE2 was the most accurate analysis. These results confirm that future work should focus on flood edge IZ first during the assimilation process.

### 6 | Conclusions

In this article a new DA framework was introduced to update and improve the flood map selection within a flood forecasting system designed for FbF applications. Open access flood likelihood data derived from satellite-based SAR were used to update the flood map selection for previously non-triggered sub-catchments or IZ during a flood event. The framework was tested on the catastrophic flooding in Pakistan, August 2022 for three different scenarios.

The first scenario tested an IZ where limited useful SAR data was available due to a dense urban area. This resulted in no flood map selection following the DA. The second scenario, where two IZ contained a mix of urban and rural areas did trigger flood maps but at low return period levels, relative to neighbouring IZ that were previously triggered. This resulted in under-estimation of the flood extent. However, the analysis flood map included flooding across parts of the city of Larkana. Information from the flood likelihood data from other areas of the IZ could select a flood map that included urban flooding. This is useful for FbF applications where population impacts are considered. The final scenario examined flood edge locations and these gave the best results as the variation in flood extent selected higher return period flood maps that were more closely matched to the validation data. The skilful scale of the analysis flood maps in the flood edge IZ was 225-525 m. Out of the 5 IZ tested, 4 resulted in a flood map selection with the dense urban area and limited SAR coverage the exception. Each of these 4 IZ were non-triggered, and now they are, which is beneficial, even if the extents are not perfect.

The non-triggered flood maps could be updated quickly following the production of the GFM flood likelihood layer (approximately 8-h after SAR acquisition). Although observed flood extent is used in the assimilation, the flood maps selected contain depth values that are already linked to a catastrophe risk model and population impact maps. Therefore the analysis is suitable to inform secondary financing schemes for flood response and recovery, during an event. In this application the entire flood map library was analysed using variational minimisation. For operational applications across a wider area, optimal iteration methods could be used to save computation time and storage. Improvements could also be made by the inclusion of prior information from the simulation library system. Currently, within the flood forecasting system, the IZ flood maps are spatially

independent of each other. Adding an additional background term in the DA framework could improve the consistency of the flood maps selected across a region and help prevent water level discrepancies across the boundaries of IZs.

An additional benefit of the new approach is that the analysis flood map could be used in a feedback loop to update the river discharge (e.g., in the associated GloFAS grid cell). This could be useful for hydrological model calibration or in updating the initial conditions for the next forecast.

Currently the SAR-derived flood likelihood data includes both flooding from direct rainfall (pluvial or surface water flooding) as well as fluvial flooding. Flood Foresight maps are currently fluvial only, which partly explains the underestimation of flood extent seen in the analysis flood map results when compared to independent satellite-derived observations. Ideally, the system would also include pluvial flood maps that could be combined with the fluvial maps to capture all flooding impacts and to enable a more complete FbF system. Alternatively, the SARderived flooding could be separated into pluvial and fluvial drivers. This would require an up-to-date detailed digital terrain model with excellent vertical accuracy by utilising, for example, LiDAR (Light Detection and Ranging) data (Chen et al. 2017). The first option is preferable as the analysis is more likely to represent flooding as observed 'from the ground' with the FbF scheme benefiting more people impacted by flooding.

Future options for optimising the simulation library flood maps could use flood depth observations if available, including from opportunistic sources such as camera images (Vandaele et al. 2021, 2023). In this case, a conventional iterative approach (such as a gradient descent methods) could step through depth values within each individual grid cell. The resultant analysis depth map would represent the best estimate of the *true* flood extent and could be used to inform secondary insurance payments.

### **Author Contributions**

Helen Hooker: conceptualization, methodology, validation, formal analysis, writing – original draft, writing – review and editing, visualization, data curation, investigation, project administration. Sarah L. Dance: conceptualization, funding acquisition, writing – review and editing, supervision, methodology, project administration. David C. Mason: conceptualization, methodology, writing – review and editing, project administration, supervision. John Bevington: supervision, project administration, writing – review and editing. Kay Shelton: supervision, data curation, project administration, writing – review and editing.

### **Conflicts of Interest**

The authors declare no conflicts of interest.

### **Data Availability Statement**

The data that support the findings of this study are available in GloFAS Global Flood Monitoring (GFM) at <a href="https://portal.gfm.eodc.eu/">https://portal.gfm.eodc.eu/</a>. The forecast flood maps from the JBA Flood Foresight system are commercial data used under licence for this study. SAR-derived flood layers may be downloaded from the GloFAS Global Flood Monitoring (GFM 2022). The forecast flood maps from the JBA Flood Foresight system are commercial data used under licence for this study.

Meteorological Applications, 2025

### References

Albertini, C., A. Gioia, V. Iacobellis, and S. Manfreda. 2022. "Detection of Surface Water and Floods with Multispectral Satellites." *Remote Sensing* 14: 6005.

Andreadis, K. M., and G. J. Schumann. 2014. "Estimating the Impact of Satellite Observations on the Predictability of Large-Scale Hydraulic Models." *Advances in Water Resources* 73: 44–54.

Annis, A., F. Nardi, and F. Castelli. 2022. "Simultaneous Assimilation of Water Levels From River Gauges and Satellite Flood Maps for Near-Real-Time Flood Mapping." *Hydrology and Earth System Sciences* 26: 1019–1041.

Bannister, R. N. 2008. "Review a Review of Forecast Error Covariance Statistics in Atmospheric Variational Data Assimilation. I: Characteristics and Measurements of Forecast Error Covariances." *Quarterly Journal of the Royal Meteorological Society* 134: 1951–1970.

Bannister, R. N. 2017. "A Review of Operational Methods of Variational and Ensemble-Variational Data Assimilation." *Quarterly Journal of the Royal Meteorological Society* 143: 607–633.

Bauer-Marschallinger, B., S. Cao, M. E. Tupas, et al. 2022. "Satellite-Based Flood Mapping through Bayesian Inference from a Sentinel-1 SAR Datacube." *Remote Sensing* 14: 1–28.

Boelee, L. 2022. "Evaluation of Global Flood Forecasts in Ungauged Catchments." Ph.D. thesis, The Open University, UK. http://oro.open.ac.uk/84856.

Bradbrook, K. 2006. "JFLOW: A Multiscale Two-Dimensional Dynamic Flood Model." *Water and Environment Journal* 20, no. 2: 79–86.

Chen, B., W. F. Krajewski, R. Goska, and N. Young. 2017. "Using LiDAR Surveys to Document Floods: A Case Study of the 2008 Iowa Flood." *Journal of Hydrology* 553: 338–349. https://doi.org/10.1016/j.jhydrol. 2017.08.009.

Chini, M., R. Hostache, L. Giustarini, and P. Matgen. 2017. "A Hierarchical Split-Based Approach for Parametric Thresholding of SAR Images: Flood Inundation as a Test Case." *IEEE Transactions on Geoscience and Remote Sensing* 55: 6975–6988.

Cooper, E. S., S. L. Dance, J. Garcia-Pintado, N. K. Nichols, and P. J. Smith. 2018. "Observation Impact, Domain Length and Parameter Estimation in Data Assimilation for Flood Forecasting." *Environmental Modelling & Software* 104: 199–214.

Cooper, E. S., S. L. Dance, J. García-Pintado, N. K. Nichols, and P. J. Smith. 2019. "Observation Operators for Assimilation of Satellite ObservaTions in Fluvial Inundation Forecasting." *Hydrology and Earth System Sciences* 23: 2541–2559.

Copernicus Programme. 2021. "Copernicus Emergency Management Service." Accessed September 14, 2021. https://emergency.copernicus.eu/.

Coughlan de Perez, E., B. Van Den Hurk, M. K. Van Aalst, et al. 2016. "Action-Based Flood Forecasting for Triggering Humanitarian Action." *Hydrology and Earth System Sciences* 20: 3549–3560.

Coughlan de Perez, E., B. Van Den Hurk, M. K. Van Aalst, B. Jongman, T. Klose, and P. Suarez. 2015. "Forecast-Based Financing: An Approach for Catalyzing Humanitarian Action Based on Extreme Weather and Climate Forecasts." *Natural Hazards and Earth System Sciences* 15: 895–904.

Dasgupta, A., R. Hostache, R. Ramasankaran, et al. 2021. "On the Impacts of Observation Location, Timing and Frequency on Flood Extent Assimilation Performance." *Water Resources Research* 57, no. 2: e2020WR028238.

Dasgupta, A., R. Hostache, R. A. Ramsankaran, et al. 2021. "A Mutual Information-Based Likelihood Function for Particle Filter Flood Extent Assimilation." *Water Resources Research* 57: 1–28.

DAWN. 2022. "Larkana Faces Threat of Outbreak due to Inundation." Accessed June 15, 2023. https://www.dawn.com/news/1707072.

de Moraes Frasson, R. P., M. J. Turmon, M. T. Durand, and C. H. David. 2023. "Estimating the Relative Impact of Measurement, Parameter, and Flow Law Errors on Discharge from the Surface Water and Ocean Topography Mission." *Journal of Hydrometeorology* 24: 425–443. https://doi.org/10.1175/JHM-D-22-0078.1.

Dey, S. R., G. Leoncini, N. M. Roberts, R. S. Plant, and S. Migliorini. 2014. "A Spatial View of Ensemble Spread in Convection Permitting Ensembles." *Monthly Weather Review* 142: 4091–4107.

Di Mauro, C., R. Hostache, P. Matgen, et al. 2021. "Assimilation of ProbAbilistic Flood Maps From SAR Data Into a Coupled Hydrologic-Hydraulic Forecasting Model: A Proof of Concept." *Hydrology and Earth System Sciences* 25: 4081–4097.

Di Mauro, C., R. Hostache, P. Matgen, et al. 2022. "A Tempered Particle Filter to Enhance the Assimilation of SAR-Derived Flood Extent Maps Into Flood Forecasting Models." *Water Resources Research* 58: e2022WR031940.

Dunning, P. 2019. "FLY." Accessed January 20, 2023. https://www.jbarisk.com/products/catastrophe-models/.

Floodlist. 2022. "Pakistan – Almost 1,000 Dead, 33 Million Affected in Worst Floods in a Decade." Accessed May 23, 2023. https://floodlist.com/asia/pakistan-floods-update-august-2022.

Frasson, R. P. d. M., G. J.-P. Schumann, A. J. Kettner, G. R. Brakenridge, and W. F. Krajewski. 2019. "Will the Surface Water and Ocean Topography (SWOT) Satellite Mission Observe Floods?" *Geophysical Research Letters* 46: 10435–10445. https://doi.org/10.1029/2019GL084686.

García-Pintado, J., D. C. Mason, S. L. Dance, et al. 2015. "Satellite-Supported Flood Forecasting in River Networks: A Real Case Study." *Journal of Hydrology* 523: 706–724.

García-Pintado, J., J. C. Neal, D. C. Mason, S. L. Dance, and P. D. Bates. 2013. "Scheduling Satellite-Based SAR Acquisition for Sequential Assimilation of Water Level Observations Into Flood Modelling." *Journal of Hydrology* 495: 252–266.

Giustarini, L., R. Hostache, D. Kavetski, et al. 2016. "Probabilistic Flood Mapping Using Synthetic Aperture Radar Data." *IEEE Transactions on Geoscience and Remote Sensing* 54: 6958–6969.

GloFAS. 2021. "GloFAS Methods." Accessed November 15, 2021. https://www.globalfloods.eu/general-information/glofas-methods/.

GloFAS Global Flood Monitoring (GFM), Accessed October 28, 2021. https://www.globalfloods.eu/technical-information/glofas-gfm/. 2021.

GloFAS Global Flood Monitoring (GFM). 2022. "Portal." https://portal.gfm.eodc.eu/login?redirect=%5Bobject%20Object%5D.

Grimaldi, S., Y. Li, V. R. Pauwels, and J. P. Walker. 2016. "Remote Sensing-Derived Water Extent and Level to Constrain Hydraulic Flood Forecasting Models: Opportunities and Challenges." *Surveys in Geophysics* 37: 977–1034.

Hooker, H., S. L. Dance, D. C. Mason, J. Bevington, and K. Shelton. 2022. "Spatial Scale Evaluation of Forecast Flood Inundation Maps." *Journal of Hydrology* 612: 128170. https://doi.org/10.1016/j.jhydrol. 2022.128170.

Hooker, H., S. L. Dance, D. C. Mason, J. Bevington, and K. Shelton. 2023a. "Assessing the Spatial Spread–Skill of Ensemble Flood Maps With Remote-Sensing Observations." *Natural Hazards and Earth System Sciences* 23: 2769–2785.

Hooker, H., S. L. Dance, D. C. Mason, J. Bevington, and K. Shelton. 2023b. "A Multi-System Comparison of Forecast Flooding Extent Using a Scale-Selective Approach." *Hydrology Research* 54: 1115–1133.

Hostache, R., M. Chini, L. Giustarini, et al. 2018. "Near-Real-Time Assimilation of SAR-Derived Flood Maps for Improving Flood Forecasts." *Water Resources Research* 54: 5516–5535.

Justice, C. O., J. R. G. Townshend, E. F. Vermote, et al. 2002. "An Overview of MODIS Land Data Processing and Product Status." *Remote Sensing of Environment* 83: 3–15. https://doi.org/10.1016/S0034-4257(02)00084-6.

Krullikowski, C., C. Chow, M. Wieland, et al. 2023. "Estimating Ensemble Likelihoods for the Sentinel-1-Based Global Flood Monitoring Product of the Copernicus Emergency Management Service." *IEEE Journal of Selected Topics in Applied Earth Observations and Remote Sensing* 16: 6917–6930.

Lai, X., Q. Liang, H. Yesou, and S. Daillet. 2014. "Variational Assimilation of Remotely Sensed Flood Extents Using a 2-D Flood Model." *Hydrology and Earth System Sciences* 18: 4325–4339.

Lauritzen, S. 2023. Fundamentals of Mathematical Statistics. Chapman and Hall/CRC.

Lehner, B. 2014. "HydroBASINS Global Watershed Boundaries and Sub-Basin Delineations Derived From HydroSHEDS Data at 15 Second Resolution." Accessed November 5, 2022. https://www.hydrosheds.org/images/inpages/HydroBASINS TechDoc vlc.pdf.

Lorenc, A. C., S. P. Ballard, R. S. Bell, et al. 2000. "The Met. Office Global Three-Dimensional Variational Data Assimilation Scheme." *Quarterly Journal of the Royal Meteorological Society* 126: 2991–3012. https://doi.org/10.1002/qj.49712657002.

Martinis, S., J. Kersten, and A. Twele. 2015. "A Fully Automated TerraSAR-X Based Flood Service." *ISPRS Journal of Photogrammetry and Remote Sensing* 104: 203–212.

Mason, D. C., I. J. Davenport, J. C. Neal, G. J. Schumann, and P. D. Bates. 2012. "Near Real-Time Flood Detection in Urban and Rural Areas Using High-Resolution Synthetic Aperture Radar Images." *IEEE Transactions on Geoscience and Remote Sensing* 50, no. 8: 3041–3052.

Mason, D. C., M. S. Horritt, J. T. Dall'Amico, T. R. Scott, and P. D. Bates. 2007. "Improving River Flood Extent Delineation From Synthetic Aperture Radar Using Airborne Laser Altimetry." *IEEE Transactions on Geoscience and Remote Sensing* 45: 3932–3943.

Matthews, G., C. Barnard, H. Cloke, et al. 2022. "Evaluating the Impact of Post-Processing Medium-Range Ensemble Streamflow Forecasts From the European Flood Awareness System." *Hydrology and Earth System Sciences* 26: 2939–2968.

Nanditha, J. S., A. P. Kushwaha, R. Singh, et al. 2023. "The Pakistan Flood of August 2022: Causes and Implications, Earth's." *Future* 11: e2022EF003. https://doi.org/10.1029/2022EF003230.

News, S. 2022. "Pakistan Floods: Satellite Images and Maps Show Scale of Disaster." Accessed August 23, 2023. https://news.sky.com/story/pakistan-floods-satellite-images-and-maps-show-scale-of-disaster-12685468.

Nguyen, T. H., S. Ricci, A. Piacentini, et al. 2023. "Assimilation of SAR-Derived Flood Extent Observations for Improving Fluvial Flood Forecast – A Proof-of-Concept." *IOP Conference Series: Earth and Environmental Science* 1136: 012018.

Pörtner, H.-O., D. Roberts, H. Adams, et al. 2022. Climate Change 2022: Impacts, Adaptation and Vulnerability, Technical Summary. Cambridge University Press.

Pujol, L., P.-A. Garambois, and J. Monnier. 2022. "Multi-Dimensional Hydrological–Hydraulic Model With Variational Data Assimilation for River Networks and Floodplains." *Geoscientific Model Development* 15: 6085–6113.

Revilla-Romero, B., K. Shelton, E. Wood, et al. 2017. "Flood Foresight: A Near-Real Time Flood Monitoring and Forecasting Tool for Rapid and Predictive Flood Impact Assessment." In EGU General Assembly Conference Abstracts, EGU General Assembly Conference Abstracts, 1230.

Revilla-Romero, B., N. Wanders, P. Burek, P. Salamon, and A. de Roo. 2016. "Integrating Remotely Sensed Surface Water Extent Into Continental Scale Hydrology." *Journal of Hydrology* 543: 659–670.

Roberts, N. M., and H. W. Lean. 2008. "Scale-Selective Verification of Rainfall Accumulations From High-Resolution Forecasts of Convective Events." *Monthly Weather Review* 136: 78–97.

Schumann, G., L. Giustarini, A. Tarpanelli, B. Jarihani, and S. Martinis. 2023. "Flood Modeling and Prediction Using Earth Observation Data." *Surveys in Geophysics* 44: 1553–1578. https://doi.org/10.1007/s10712-022-09751-y.

Speight, L. J., M. D. Cranston, C. J. White, and L. Kelly. 2021. "Operational and Emerging Capabilities for Surface Water Flood Forecasting." *Wiley Interdisciplinary Reviews: Water* 8: 1–24.

Start Network. 2022. "Anticipation and Risk Financing." Accessed October 25, 2022. https://startnetwork.org/anticipation-and-risk-financing.

Stephens, E., and H. Cloke. 2014. "Improving Flood Forecasts for Better Flood Preparedness in the UK (and Beyond)." *Geographical Journal* 180: 310–316.

Stephens, E., G. Schumann, and P. Bates. 2014. "Problems With Binary Pattern Measures for Flood Model Evaluation." *Hydrological Processes* 28: 4928–4937. https://doi.org/10.1002/hyp.9979.

The Guardian. 2022. "Pakistan Floods Cause Devastation – In Pictures." Accessed June 15, 2023. https://www.theguardian.com/world/gallery/2022/aug/30/pakistan-floods-cause-devastation-in-pictures.

Twele, A., W. Cao, S. Plank, and S. Martinis. 2016. "Sentinel-1-Based Flood Mapping: A Fully Automated Processing Chain." *International Journal of Remote Sensing* 37: 2990–3004.

Vandaele, R., S. L. Dance, and V. Ojha. 2021. "Deep Learning for Automated River-Level Monitoring Through River-Camera Images: An Approach Based on Water Segmentation and Transfer Learning." *Hydrology and Earth System Sciences* 25: 4435–4453.

Vandaele, R., S. L. Dance, and V. Ojha. 2023. "Calibrated River-Level Estimation From River Cameras Using Convolutional Neural Networks." *Environmental Data Science* 2: e11.

Wagner, W., V. Freeman, S. Cao, et al. 2020. "Data Processing Architectures For Monitoring Floods Using Sentinel-1, ISPRS Annals of the Photogrammetry, Remote Sensing and Spatial." *Information Sciences* V-3-2020: 641–648.

World Resources Institute. 2023. "How Floods in Pakistan Threaten Global Security." Accessed August 23, 2023. https://www.wri.org/insig hts/pakistan-floods-threaten-global-security#:~:text=In%20Pakistan% 2C%20torrential%20rains%20and,and%20killed%20over%20900% 2C000%20livestock.

World Weather Attribution. 2022. "Climate Change Likely Increased Extreme Monsoon Rainfall, Flooding Highly Vulnerable Communities in Pakistan." Accessed August 23, 2022. https://www.worldweatheratt ribution.org/climate-change-likely-increased-extreme-monsoon-rainf all-flooding-highly-vulnerable-communities-in-pakistan/.

Wu, W., R. Emerton, Q. Duan, A. W. Wood, F. Wetterhall, and D. E. Robertson. 2020. "Ensemble Flood Forecasting: Current Status and Future Opportunities." *WIREs Water* 7: 1–32.

Meteorological Applications, 2025